

Numerical investigation of the non-Newtonian pulsatile blood flow in a bifurcation model with a non-planar branch

Jie Chen, Xi-Yun Lu*

Department of Modern Mechanics, University of Science and Technology of China, 96 Jin-Zhai Road, Hefei, Anhui 230026, PR China

Accepted 7 February 2005

Abstract

The pulsatile flow of non-Newtonian fluid in a bifurcation model with a non-planar daughter branch is investigated numerically by using the Carreau–Yasuda model to take into account the shear thinning behavior of the analog blood fluid. The objective of this study is to deal with the influence of the non-Newtonian property of fluid and of out-of-plane curvature in the non-planar daughter vessel on wall shear stress (WSS), oscillatory shear index (OSI), and flow phenomena during the pulse cycle. The non-Newtonian property in the daughter vessels induces a flattened axial velocity profile due to its shear thinning behavior. The non-planarity deflects flow from the inner wall of the vessel to the outer wall and changes the distribution of WSS along the vessel, in particular in systole phase. Downstream of the bifurcation, the velocity profiles are shifted toward the flow divider, and low WSS and high shear stress temporal oscillations characterized by OSI occur on the outer wall region of the daughter vessels close to the bifurcation. Secondary motions become stronger with the addition of the out-of-plane curvature induced by the bending of the vessel, and the secondary flow patterns swirl along the non-planar daughter vessel. A significant difference between the non-Newtonian and the Newtonian pulsatile flow is revealed during the pulse cycle; however, reasonable agreement between the non-Newtonian and the rescaled Newtonian flow is found. Calculated results for the pulsatile flow support the view that the non-planarity of blood vessels and the non-Newtonian properties of blood are an important factor in hemodynamics and may play a significant role in vascular biology and pathophysiology.

© 2005 Elsevier Ltd. All rights reserved.

Keywords: Non-Newtonian fluid flow; Pulsatile flow; Non-planar artery; Carotid bifurcation; Hemodynamics

1. Introduction

Hemodynamics is thought to play an important role for the localization of vascular disease in areas of complex flow in the coronary, carotid, abdominal, and femoral arteries. These complex flow regions often occur due to branching, bifurcation, and curvature of the arteries. A variety of hemodynamic factors have been implicated in the development of atherosclerosis, including disturbed flow patterns (Hughes and How, 1995; Staalsen et al., 1995), low shear stress (Dobrin

et al., 1989; White et al., 1993; Delfino et al., 1997), low and oscillating shear (Bassiouny et al., 1992; Taylor et al., 1998, 1999), temporal variation of the shear stress (Ojha, 1994), spatial wall shear stress gradient (Klein-streuer et al., 1996; Lei et al., 1997), and wall tension (Schwartz et al., 1992; Hofer et al., 1996). Meanwhile, it is noted that there exist three risk factors for the development of atherogenesis (Araim et al., 2001), which include low shear stress region, high vessel pressure distribution, and high particle residence time in the region of atherosclerosis.

It is well known that specific sites in the arterial tree are sensitive to the development of atherosclerotic lesions (Caro et al., 1971; Friedman et al., 1981; Zarins et al., 1983; Nerem, 1992). Usually, local hemodynamics

*Corresponding author. Tel.: +86 551 3603223;
fax: +86 551 3606459.

E-mail address: xlu@ustc.edu.cn (X.-Y. Lu).

is not only governed by the geometry of the bifurcation and the properties of the arterial wall, but also by the rheological properties of blood. Meanwhile, the non-planarity of the artery is also an important factor influencing arterial flows, and the curvature of the aortic arch is approximately helical (Caro et al., 1996). In addition to these factors, pulsatile flow in vascular vessel has a significant influence on hemodynamic behaviors and is particularly complex (Taylor et al., 1998, 1999).

Researchers have performed a lot of work on blood flow in order to disclose the reason of the atherogenesis theoretically (e.g., Sarkar and Jayaraman, 1998) and experimentally (e.g., Zhao et al., 2000; Ding et al., 2001). However, the theoretical analysis was limited to deal with some simple problem, while the experiment was time-consuming and costly. Thus, based on the computational fluid dynamics methods, some work has been performed, including the non-Newtonian blood flow (Lou and Yang, 1993), the pulsatile flow (Tu and Deville, 1996; Zendehebudi and Moayeri, 1999), the three-dimensional complex geometries (Hofer et al., 1996; Santamarina et al., 1998; Weydahl and Moore, 2001; Lee et al., 2001; Lu et al., 2002), multi-branch (Shipkowitz et al., 1998), and even reconstructed from the realistic artery with the data from the experiment (Friedman and Ding, 1998; Perktold et al., 1998; Weston et al., 1998). But the conditions mentioned above are considered separately and the influence of the conditions has not been well analyzed. Recently, the present authors (Lu et al., 2002; Chen and Lu, 2004) have studied the influence of non-Newtonian fluid properties and non-planarity of an arterial bifurcation on the flow and wall shear stress (WSS). However, to the authors' knowledge, little work has been performed to investigate the pulsatile flow of non-Newtonian fluid in a bifurcation model with a non-planar daughter branch; thus it motivates us to carry out the present study based on our previous work (Lu et al., 2002; Chen and Lu, 2004).

Here, the pulsatile flow of non-Newtonian fluid on the velocity distribution, WSS, and shear stress temporal oscillation in a non-planarity artery with bifurcation is investigated. The three-dimensional incompressible Navier–Stokes equations coupled with the non-Newtonian constitutive model are numerically solved by a time-accurate finite element method. To compare the flow behavior of the non-Newtonian fluid with that of the Newtonian fluid, calculated results for the Newtonian fluid with the original Reynolds number and the corresponding rescaled Reynolds number are given. Based on our calculated results, the influence of the non-planarity of the blood vessel and the non-Newtonian properties of the blood on the pulsatile flow through three-dimensional artery bifurcation is discussed.

2. Methods

The governing equations are the three-dimensional incompressible Navier–Stokes equations and are given as

$$\rho \left(\frac{\partial \mathbf{u}}{\partial t} + \mathbf{u} \cdot \nabla \mathbf{u} \right) = -\nabla p + \nabla \cdot \mathbf{T}, \quad (1)$$

where \mathbf{u} is the fluid velocity vector, ρ the density and p the pressure. \mathbf{T} is the stress tensor and linearly dependent on the rate of deformation tensor \mathbf{D} with a relation of $\mathbf{T} = 2\eta(\dot{\gamma})\mathbf{D}$, where $\mathbf{D} = \frac{1}{2}(\nabla \mathbf{u} + \nabla \mathbf{u}^T)$, η represents the viscosity of the blood, and $\dot{\gamma}$ is the shear rate. For a non-Newtonian fluid, η is a function of $\dot{\gamma}$, while for a Newtonian fluid η is a constant and independent of the shear rate $\dot{\gamma}$. The divergence-free condition is imposed on the velocity \mathbf{u} :

$$\nabla \cdot \mathbf{u} = 0. \quad (2)$$

Here, we consider blood as a non-Newtonian fluid. The shear thinning and viscoelasticity of blood (Chien et al., 1970; Thurston, 1973, 1979) are related to its microscopic structures, e.g., aggregation, deformation and alignment of the red blood cells, where the red blood cells determine mainly the rheological behavior of blood. Investigation of non-Newtonian steady flow in a carotid bifurcation model indicates that the shear thinning is the dominant non-Newtonian property of the blood (Gijssen et al., 1999a, b). In this specific case, there is an indication that viscoelastic properties may be ignored, even though the importance of the viscoelasticity of the blood analog fluids on the flow phenomena has been presented by Liepsch and Moravec (1984) and Ku and Liepsch (1986). In the present study, the Carreau–Yasuda shear thinning model (Bird et al., 1987) was used,

$$\frac{\eta - \eta_\infty}{\eta_0 - \eta} = [1 + (\lambda \dot{\gamma})^a]^{(n-1)/a}, \quad (3)$$

where $\dot{\gamma}$ represents a scalar quantity of the rate of deformation tensor, defined as $\dot{\gamma} = \sqrt{2\text{tr}(\mathbf{D}^2)}$ and $D = [\nabla \mathbf{u} + (\nabla \mathbf{u})^T]/2$. The other parameters in Eq. (3) are obtained from experimental data based on the analog blood fluid (Gijssen et al., 1999a, b) and expressed as $\eta_\infty = 2.2 \times 10^{-3}$ Pa s, $\eta_0 = 22 \times 10^{-3}$ Pa s, $\lambda = 0.110$ s, $a = 0.644$, $n = 0.392$ and $\rho = 1410$ kg/m³.

To compare the behavior of the non-Newtonian and Newtonian pulsatile flow, calculations were also performed using the Newtonian fluid employed by Gijssen et al. (1999b). Based on the experimental data of the analog blood fluid (Gijssen et al., 1999a, b), a concentrated solution of potassium thiocyanate in water (KSCN, 71% by weight) was employed as the Newtonian control fluid with the initial Newtonian viscosity $\eta = 2.9 \times 10^{-3}$ Pa s.

Further, to define a rescaled Reynolds number, a characteristic shear rate (i.e., $\dot{\gamma}_c$) is needed. The characteristic shear rate for the blood flow in larger arteries can be defined in various ways. Some authors use the wall shear rate (e.g., Mann and Tarbell, 1990; Cho and Kensey, 1991), which in fact is often the highest shear rate occurring in blood flow, while others use the average shear rate (e.g., Ballyk et al., 1994; Baaijens et al., 1993; Thurston, 1979). Here, as used by Thurston (1973, 1979), Gijsen et al. (1999b), and Chen and Lu (2004), a definition of the characteristic shear rate is given as

$$\dot{\gamma}_c = \frac{2V}{a}, \tag{4}$$

where V and a represent the mean velocity at the inlet of mother tube and the radius of the mother tube. Using the above-mentioned parameters (Gijsen et al., 1999a, b), the rescaled Reynolds number can be calculated.

A close correlation between intimal thickening and oscillations in shear characterized by an oscillatory shear index (OSI) has been noted by Ku et al. (1985). To introduce the OSI, some quantities relevant to the surface traction need to be described. The traction vector can be computed from the stress tensor (σ) and surface normal vector (\mathbf{n}) by $\mathbf{t} = \sigma\mathbf{n}$, and the surface traction vector, \mathbf{t}_s , defined as the tangential component

of the traction vector, can be computed from $\mathbf{t}_s = \mathbf{t} - (\mathbf{t} \cdot \mathbf{n})\mathbf{n}$. Then, the OSI is defined as (Taylor et al., 1998, 1999)

$$OSI = \frac{1}{2} \left(1 - \frac{\tau_{\text{mean}}}{\tau_{\text{mag}}} \right), \tag{5}$$

where τ_{mean} represents the mean shear stress to express the magnitude of the time-averaged surface traction vector and τ_{mag} is the time-averaged magnitude of the surface traction vector. They are defined as, respectively,

$$\tau_{\text{mean}} = \left| \frac{1}{T} \int_0^T \mathbf{t}_s \, dt \right|, \quad \tau_{\text{mag}} = \frac{1}{T} \int_0^T |\mathbf{t}_s| \, dt. \tag{6}$$

Fig. 1 shows a hypothetical three-dimensional non-planar artery with bifurcation which was used in our previous work (Lu et al., 2002; Chen and Lu, 2004). The configuration model is demonstrated in Figs. 1(a)–1(c). In this model, the mother vessel and the daughter vessels have the same diameter (D). The mother vessel has a length of $3D$. The bifurcation is symmetric and planar and the bifurcating angle is 90° . One daughter vessel is straight with a length of $8D$, and the other one is straight planar $1.5D$ along the axial and then undergoes 45° bending with a radius of $4D$ before it straightens up for a further length of $4D$.

The flow waveform with period $T = 1$ s, which was used experimentally by Gijsen et al. (1999b), at the inlet

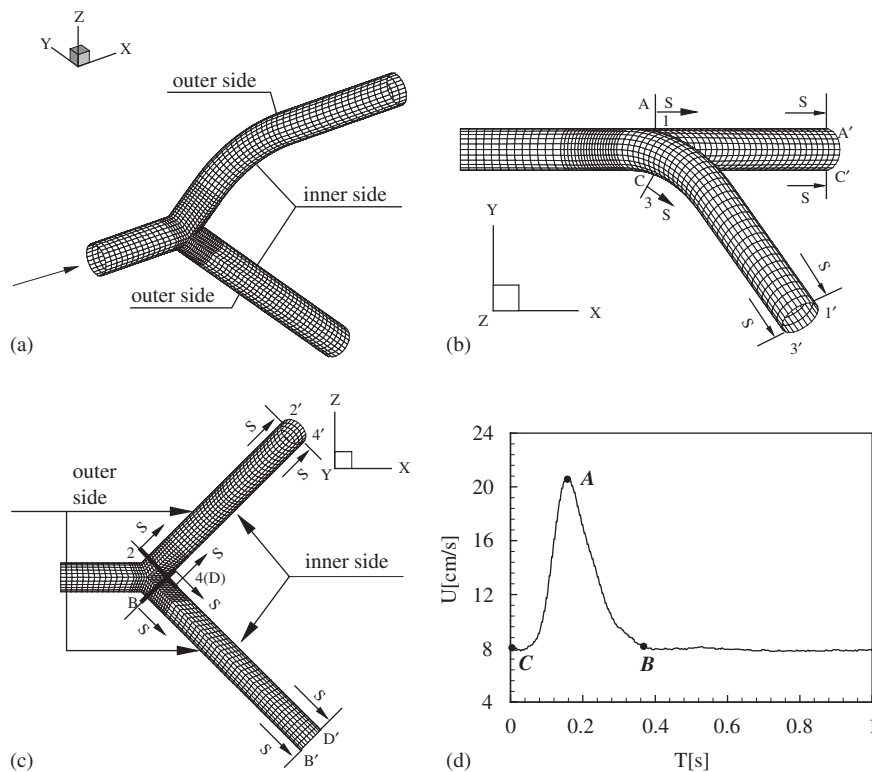


Fig. 1. Geometry of three-dimensional bifurcation model with a non-planar daughter branch: (a) global view; (b) view face to z-direction; (c) view from y-direction; (d) mean axial velocity during the pulse cycle.

of mother vessel with the diameter $D = 8$ mm is shown in Fig. 1(d). The mean axial velocity (V) at the inlet of the mother tube is a function of time. Then, the Reynolds number for the Newtonian fluid flow, defined as $Re = \rho DV/\eta$, varies from about 300 (diastole) to 750 (peak systole), while the Womersley number based on the period of the flow pulse is equal to 7.

As proposed by Weydahl et al. (2001), Lu et al. (2002), and Chen and Lu (2004), the initial velocity in the whole field is assumed to be zero. At the inlet, the Womersley boundary conditions with time-dependent axisymmetric velocity profiles are imposed. The velocity conditions obey the no-slip constraint on the walls. At the exit of each daughter vessel, a fully developed flow is assumed and a zero axial velocity gradient is employed. Meanwhile, a zero axial pressure gradient is used at the exit of the planar daughter vessel, while a zero reference pressure is set at the exit of the non-planar one.

A time-accurate finite element method based on a fractional-step velocity correction (Kovacs and Kawahara, 1991; Lu et al., 2002; Chen and Lu, 2004; Wang et al., 2004) is applied to solve Eqs. (1) and (2). The finite element spatial discretization is performed using the Galerkin weighted residual method. The discretized formulation was described by Kovacs and Kawahara (1991) in detail.

3. Results

To validate the present calculation, a pulsatile flow of non-Newtonian fluid in a 90° curved tube with the flow pulse shown in Fig. 1(d), which was investigated by Gijzen et al. (1999b), is calculated. Fig. 2 shows the axial velocity profiles in the plane of symmetry and perpendicular to this plane for the non-Newtonian fluid described in Eq. (3) at peak systole (i.e., location A in Fig. 1(d)), beginning of diastole (B), and end of diastole (C), respectively. The corresponding experimental and numerical results obtained by Gijzen et al. (1999b) are plotted in Fig. 2. The present results are in quite good agreement with those experimental and numerical data. Further, the present computational code has also been verified in our previous study (Lu et al., 2002; Wang et al., 2004).

3.1. Axial velocity profiles

3.1.1. Peak systole

The profiles of the axial velocity along the daughter vessel in the bending and bifurcation plane at peak systole (i.e., location A in Fig. 1(d)) are shown in Fig. 3. During systole, the inertia forces, taking account for the acceleration of the fluid, dominate the flow features. The mean velocity reaches a maximum at peak systole. Thus,

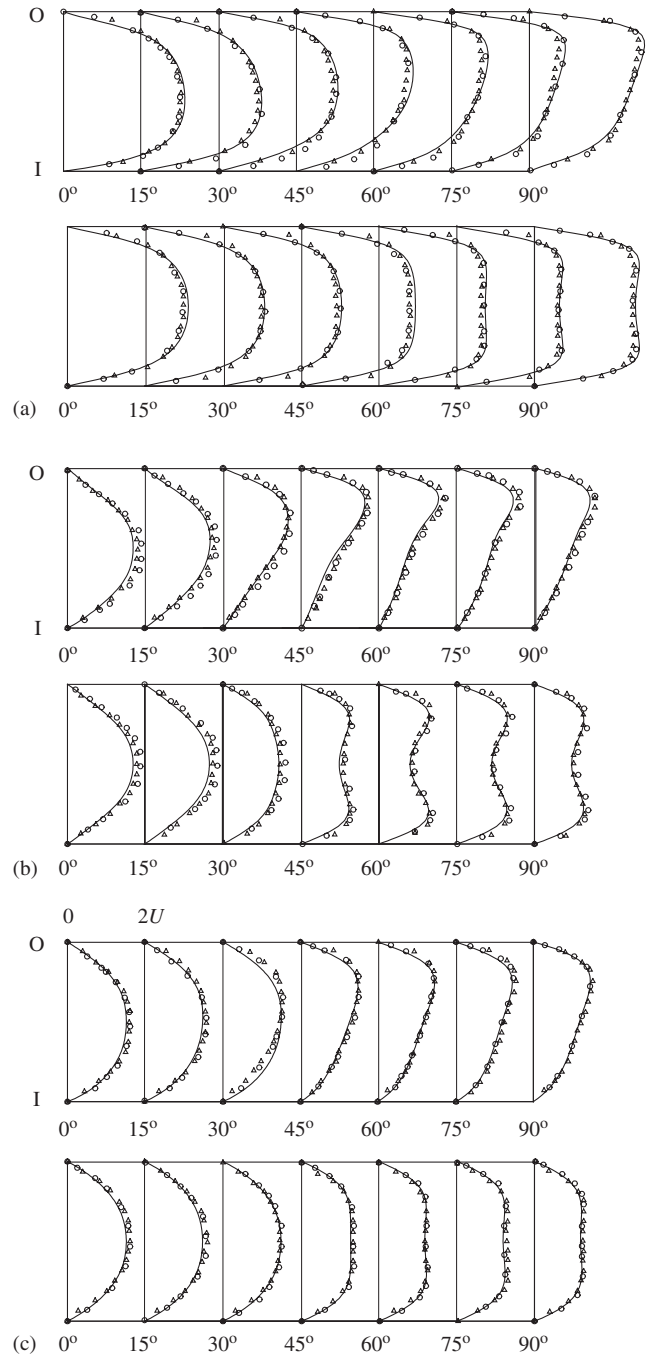


Fig. 2. Axial velocity profiles in the plane of symmetry (top) and perpendicular to this plane (bottom) for the non-Newtonian fluid and comparison with the experimental and numerical results. Here, symbols Δ and \circ denote the experimental and numerical data given by Gijzen et al. (1999b), and the solid line means the present result. I and O denote the inner and outer wall of the curved tube. (a) Peak systole; (b) beginning of diastole; (c) end of diastole.

the viscous boundary layer becomes much thinner, resulting in steep velocity gradients near the wall.

To view the axial velocity profiles in the bending plane along the planar vessel in Fig. 3(a) and along the non-planar vessel in Fig. 3(c), typical M-shaped velocity

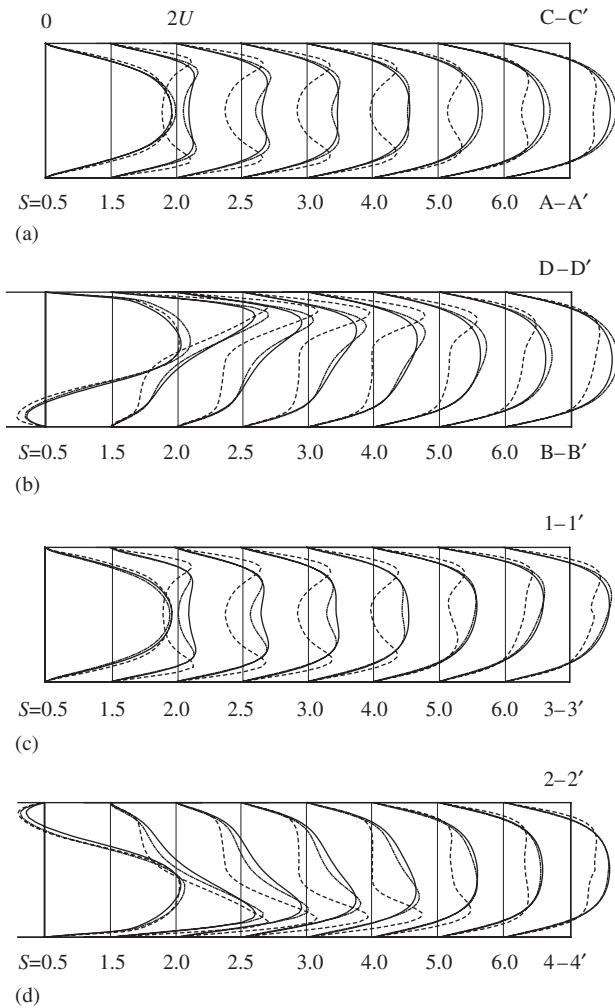


Fig. 3. Axial velocity profiles along the vessels in the bending plane and in the bifurcation plane at peak systole for the non-Newtonian (solid line), Newtonian (dashed line), and rescaled Newtonian fluid flow (dash-dot line): (a) A–A' and C–C'; (b) B–B' and D–D'; (c) 1–1' and 3–3'; (d) 2–2' and 4–4'. Here, U denotes the time-averaged value of axial velocity over the pulse cycle in Fig. 1(d). S is the distance along the generating line from the location of cross-section contour through the junction of the bifurcation, where the cross-section plane is perpendicular to the local axial direction of daughter vessels as marked in Fig. 1. U and S represent the same meaning in the following figures.

profiles are observed for the Newtonian flow and become less evident for the non-Newtonian flow due to its shear-thinning behavior. The velocity profiles are symmetric along the planar vessel in Fig. 3(a). However, as shown in Fig. 3(c), the velocity profiles are slightly skewed toward the inner wall for $S = 0.5–2.5$ due to the entrance flow influence near the entry section of the daughter vessels, and then toward the outer wall of the curved vessel along the non-planar vessel from $S = 2.5$ approximately.

The axial velocity profiles in the bifurcation plane are shown along the planar vessel in Fig. 3(b) and along the non-planar vessel in Fig. 3(d). The flow separation on

the outer walls of the vessels near the entry section of the daughter vessels is obviously formed at $S = 0.5$. Downstream of the bifurcation, the velocity profiles are seriously shifted toward the flow-dividing wall from $S = 0.5$ to 2.5 , and become flattening for the non-Newtonian fluid from $S = 3$ approximately. As shown in Fig. 3(d), the velocity profiles are slightly skewed toward the outer wall again at $S = 5$, where the non-planar-bending tube switches to the straight tube.

3.1.2. Beginning of diastole

The profiles of the axial velocity along the planar and non-planar daughter vessel at the beginning of diastole (i.e., location B in Fig. 1(d)) are shown in Fig. 4. At this stage, the adverse axial pressure gradient to decelerate the fluid flow from the peak systole to the beginning of diastole is expected to influence the axial velocity distributions.

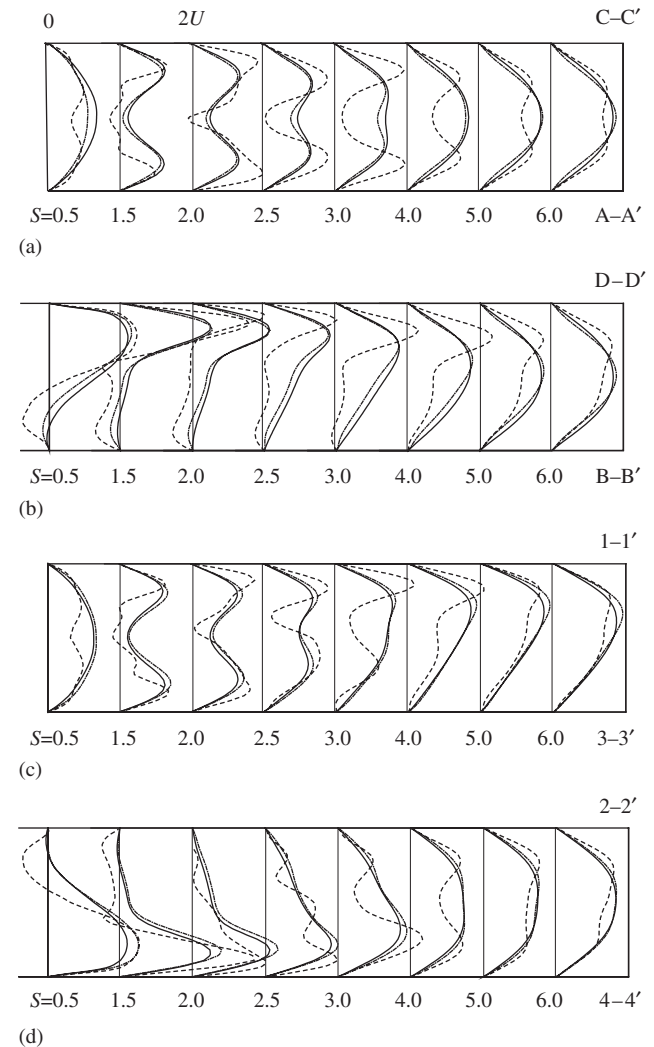


Fig. 4. Axial velocity profiles along the vessels in the bending plane and in the bifurcation plane at the beginning of diastole: (a) A–A' and C–C'; (b) B–B' and D–D'; (c) 1–1' and 3–3'; (d) 2–2' and 4–4'.

The axial velocity profiles in the bending plane are shown along the planar vessel in Fig. 4(a) and along the non-planar vessel in Fig. 4(c). The deficit velocity distributions in the central part of the daughter vessels are more pronounced, even the velocity value for the Newtonian flow being negative at $S = 1.5$ due to the adverse axial pressure gradient effect. The velocity profiles in Fig. 4(c) are skewed toward the outer wall of the curved vessel along the non-planar vessel from $S = 3$ approximately.

The corresponding axial velocity profiles in the bifurcation plane are shown along the planar vessel in Fig. 4(b) and along the non-planar vessel in Fig. 4(d). In the downstream of the bifurcation, the velocity profiles are shifted toward the flow-dividing wall and show significant flattening for the non-Newtonian fluid. The shift of the peak axial velocity toward the outer wall is more pronounced. Flow reversal is observed near the outer walls of the vessels in the region of $S \leq 1.5$. As shown in Fig. 4(d), the flow is skewed toward the flow-dividing wall. Then, due to the bending effect of the tube out of the bifurcation plane, the peak axial velocity, e.g., $S = 5$ and 6 in Fig. 4(d), deviates from the divider wall to non-divider wall in the non-planar branch.

3.1.3. End of diastole

Fig. 5 shows the profiles of the axial velocity along the daughter vessels at the end of diastole (i.e., location C in Fig. 1(d)). The axial velocity profiles in the bending plane are shown along the planar vessel in Fig. 5(a) and along the non-planar vessel in Fig. 5(c). The velocity profiles are symmetric along the planar vessel in Fig. 5(a). However, the velocity profiles are skewed toward the outer wall of the curved vessel along the non-planar vessel from $S = 2.5$ approximately. Immediately downstream of the bifurcation, M-shaped velocity profiles are observed, in particular for the Newtonian fluid. Because of the shear-thinning behavior of the non-Newtonian fluid, the velocity field is flattened and has lower velocity gradients at the inner walls and positive velocity gradients at the outer walls. Thus, the M-shaped velocity profiles of the non-Newtonian flow become less evident.

The axial velocity profiles in the bifurcation plane are shown along the planar vessel in Fig. 5(b) and along the non-planar vessel in Fig. 5(d). The velocity profiles are shifted toward the flow-dividing wall (i.e., the inner wall of the bifurcation) and exhibit significant flattening for the non-Newtonian fluid. As shown in Fig. 5(d), in the region where the non-planar-bending tube switches to the straight tube, the velocity profiles are slightly skewed toward the outer wall again at $S = 5$ approximately. Then, the velocity profile approaches asymptotically to be symmetric when the effects of curvature and bifurcation are negligible. By comparing the velocity profiles along the planar vessel in Fig. 5(b) with those

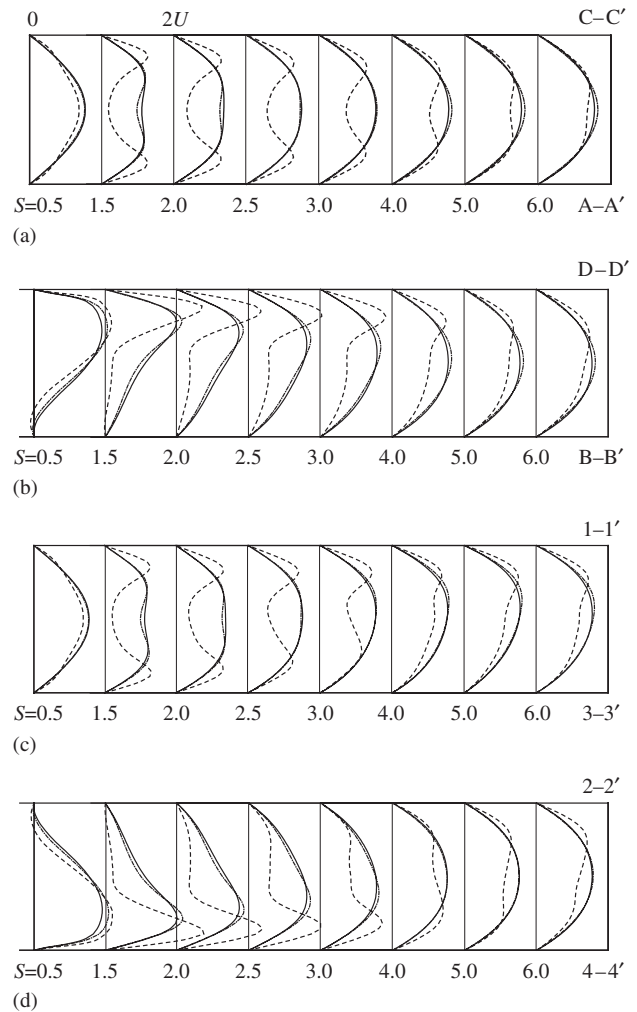


Fig. 5. Axial velocity profiles along the daughter vessels in the bending plane and in the bifurcation plane at the end of diastole: (a) A–A' and C–C'; (b) B–B' and D–D'; (c) 1–1' and 3–3'; (d) 2–2' and 4–4'.

along the non-planar vessel in Fig. 5(d), curvature variation due to the bifurcation from the mother tube induces the flow to be skewed toward the inner wall. Bending of the tube out of the bifurcation plane introduces another curvature. The superposition of the two types of curvature effects results in flow to deviate from the divider wall to non-divider wall in the non-planar branch, as shown in Fig. 5(d) for $S = 5$ and 6. The axial velocity profiles of the non-Newtonian and the rescaled Newtonian flow, compared to those of the Newtonian flow, show significant flattening and are skewed to the inner wall.

3.2. Axial velocity contours and secondary flow patterns

To exhibit the influence of the bifurcation and curvature on flow phenomena, the axial velocity contours and secondary flow patterns are further analyzed. Different features for the non-Newtonian

and Newtonian fluid flow have been discussed in our previous work (Chen and Lu, 2004). Here, we mainly pay attention to the corresponding behavior of the non-Newtonian flow during the pulse cycle. Fig. 6 shows the axial velocity contours and secondary flow streamlines along the planar daughter vessel for the non-Newtonian fluid at peak systole, beginning of diastole, and end of diastole, respectively. The crescent contours of the axial velocity change from skewed to the inner wall to a more parabolic profile with the time development from the end of diastole in Fig. 6(c), to peak systole in Fig. 6(a) and to beginning of diastole in Fig. 6(b), e.g., at $S = 1.5$, 2 and 2.5. Due to the adverse axial pressure gra-

dient effect at the beginning of diastole, C-shaped axial velocity contours appear at $S = 1.5$, 2 and 2.5 in Fig. 6(b).

Secondary flow streamlines at several sections along the planar vessel for the non-Newtonian fluid flow are shown in Fig. 6(d)–(f). There is pronounced movement of fluid from the outer wall of the bifurcation toward the inner wall. They are caused by a centripetal acceleration (or pressure gradient) introduced by the curvature in the vessel. At sections close to the bifurcation, e.g., at $S = 0.5$ and 1.5, counter-rotating vortices (i.e., Dean vortices) are evident and result in a shift of the peak axial velocity toward the flow-dividing wall during the

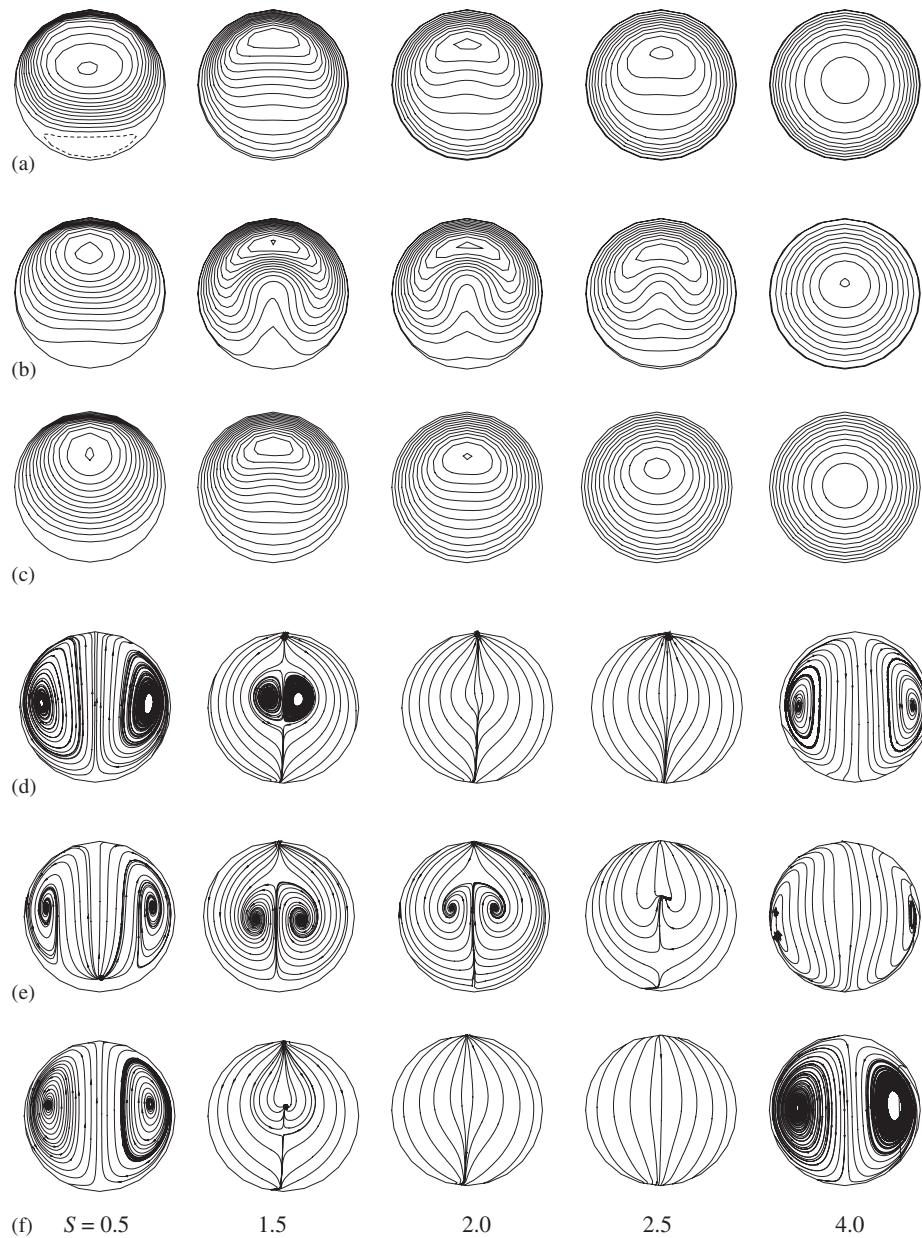


Fig. 6. Axial velocity contours (a)–(c) and secondary flow streamlines (d)–(f) along the planar daughter vessel for the non-Newtonian fluid: (a), (d) peak systole; (b), (e) beginning of diastole; (c), (f) end of diastole.

pulse cycle. The secondary vortex at peak systole in Fig. 6(d), apart from being somewhat stronger, exhibits essentially similar features as that at the end of diastole in Fig. 6(f). The strength of the Dean vortex at the beginning of diastole in Fig. 6(e), compared to that in Fig. 6(f), increases and influences significantly the axial velocity distribution, as shown in Fig. 4(a) and (b).

The axial velocity contours and secondary flow patterns along the non-planar daughter vessel for the non-Newtonian fluid are shown in Fig. 7. The crescent contours of the axial velocity are more pronounced to be skewed to the inner wall, in particular at the beginning of diastole in Fig. 7(b). The swirling effect is better illustrated in the axial velocity contours at those sections. Due to the bending effect of the tube

out of the bifurcation plane, flow deviates from the inner wall of the bifurcation to its sidewall. The crescent shape rotates along the vessel in the anti-clockwise direction viewing from the end of the daughter vessel during the pulse cycle. However, compared to the axial velocity contours for the Newtonian fluid (not shown here), the crescent shape rotation along the vessel is very weak for the non-Newtonian fluid, and an axisymmetrical pattern is gradually formed along the vessel.

As shown in Fig. 7 for the secondary flow streamlines, the flow patterns are asymmetrical, which reflects the influence of the curvature due to the out-of-plane bend. The stronger vortex gradually dominates the secondary flow field. A single recirculation zone, in particular at

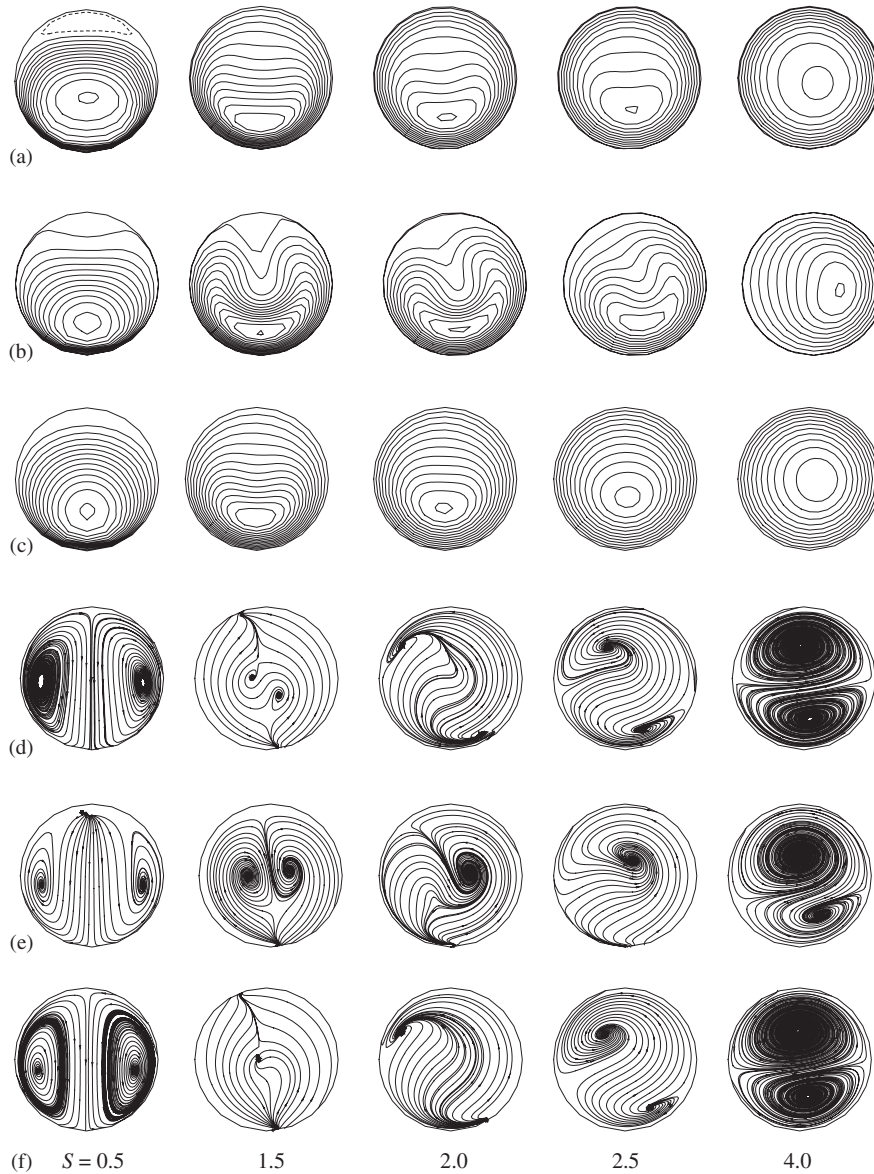


Fig. 7. Axial velocity contours (a)–(c) and secondary flow streamlines (d)–(f) along the non-planar daughter vessel for the non-Newtonian fluid: (a), (d) peak systole; (b), (e) beginning of diastole; (c), (f) end of diastole.

the beginning of diastole in Fig. 7(e), is a typical feature of non-planar flows due to torsion (Zabielky and Mestel, 1998a, b; Sherwin et al., 2000). The secondary structures at the end of diastole in Fig. 7(f) and at the peak systole in Fig. 7(d) are similar to each other, and the secondary vortices at the beginning of diastole in Fig. 7(e) are somewhat stronger.

3.3. Wall shear stress (WSS) and oscillatory shear index (OSI)

Distributions of WSS along four generating lines on the non-planar and planar daughter vessels are shown in Figs. 8–10 for peak systole, beginning of diastole and end of diastole, respectively. The results exhibit that

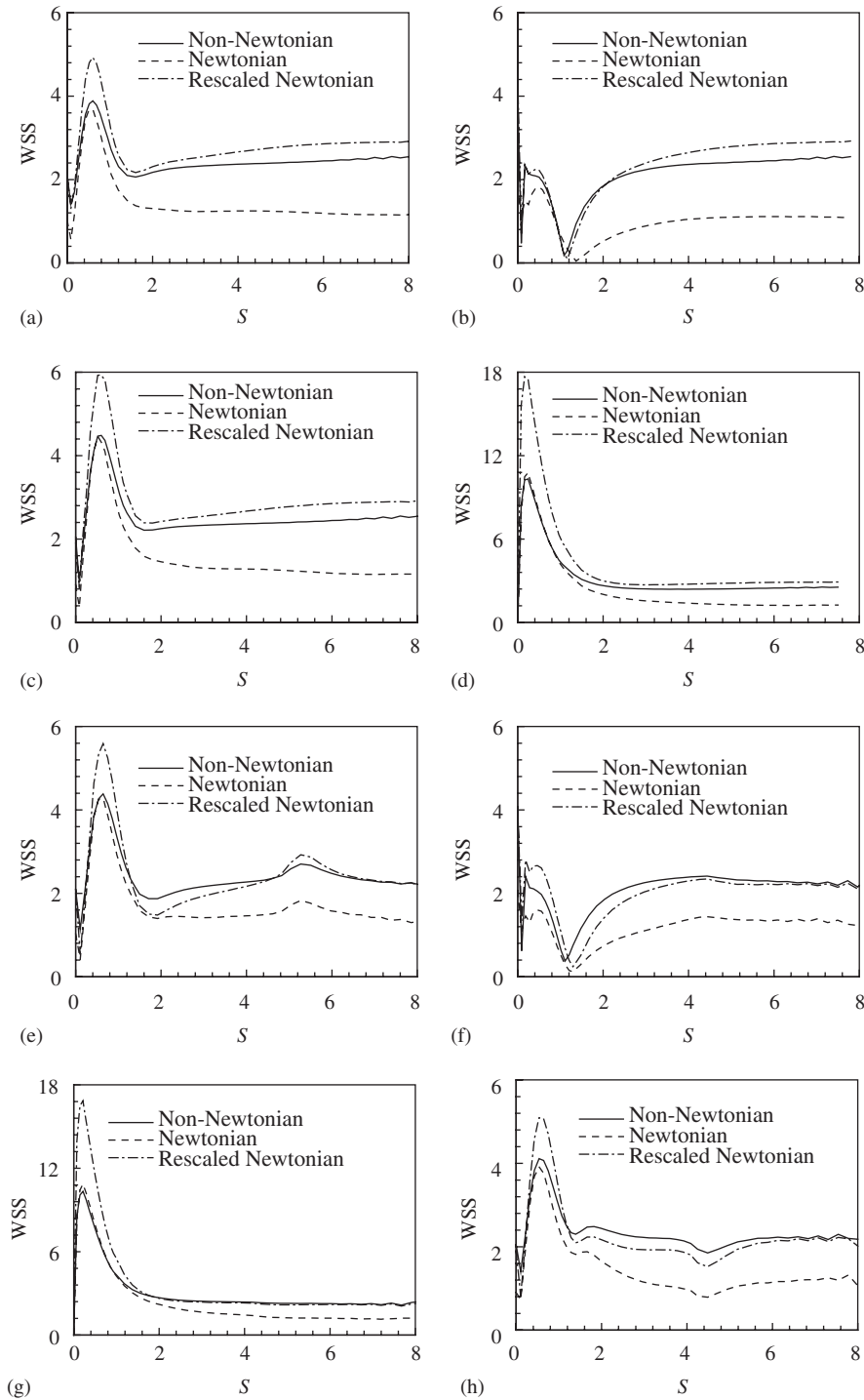


Fig. 8. Distributions of WSS along eight generating lines on the daughter vessels at peak systole for the non-Newtonian (solid line), Newtonian (dashed line) and rescaled Newtonian fluid flow (dash-dot line): (a) A–A'; (b) B–B'; (c) C–C'; (d) D–D'; (e) 1–1'; (f) 2–2'; (g) 3–3'; (h) 4–4'.

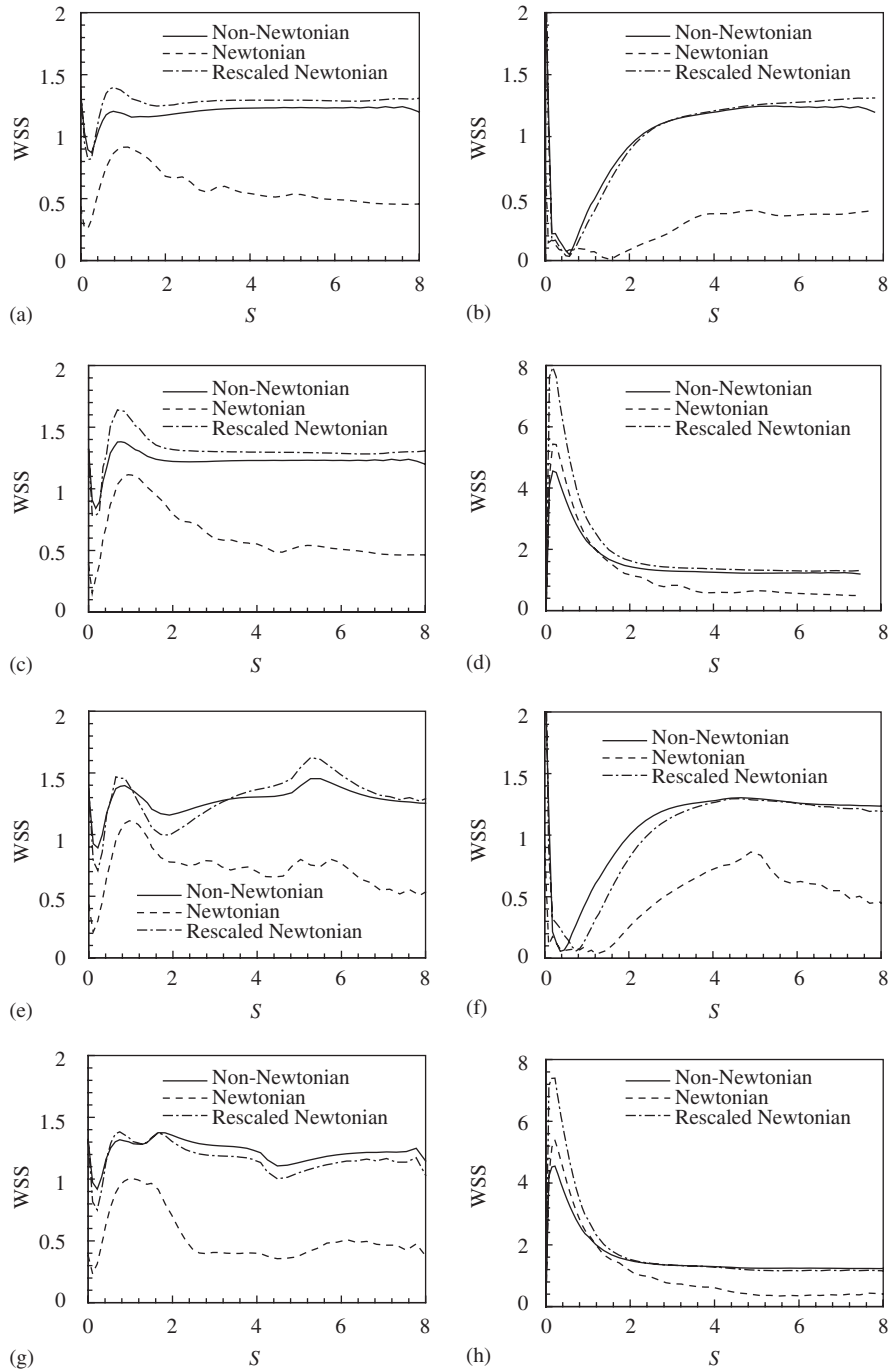


Fig. 9. Distributions of WSS along eight generating lines on the daughter vessels at the beginning of diastole: (a) A–A'; (b) B–B'; (c) C–C'; (d) D–D'; (e) 1–1'; (f) 2–2'; (g) 3–3'; (h) 4–4'.

there exists a significant difference of WSS of the non-Newtonian and Newtonian flow due to the shear-thinning effect. It is observed that the distributions of WSS on the daughter vessels at the beginning of diastole (Fig. 9) are similar to those at the end of diastole (Fig. 10). As the mean velocity reaches a maximum and the viscous boundary layer becomes much thinner at peak systole, the magnitudes of WSS profiles in Fig. 8, compared to those in Figs. 9 and 10,

are larger. Thus, as a typical case, the features of WSS on the daughter vessels at the end of diastole are mainly described.

As shown in Fig. 10, the out-of-plane bend results in the variation of WSS, but the most significant change occurs in the bending plane. At the inner wall of the bend in Fig. 10(g), the WSS over the section of the bend is reduced on average by 10–15% compared to that in the planar vessel in Fig. 10(c). However, at the outer

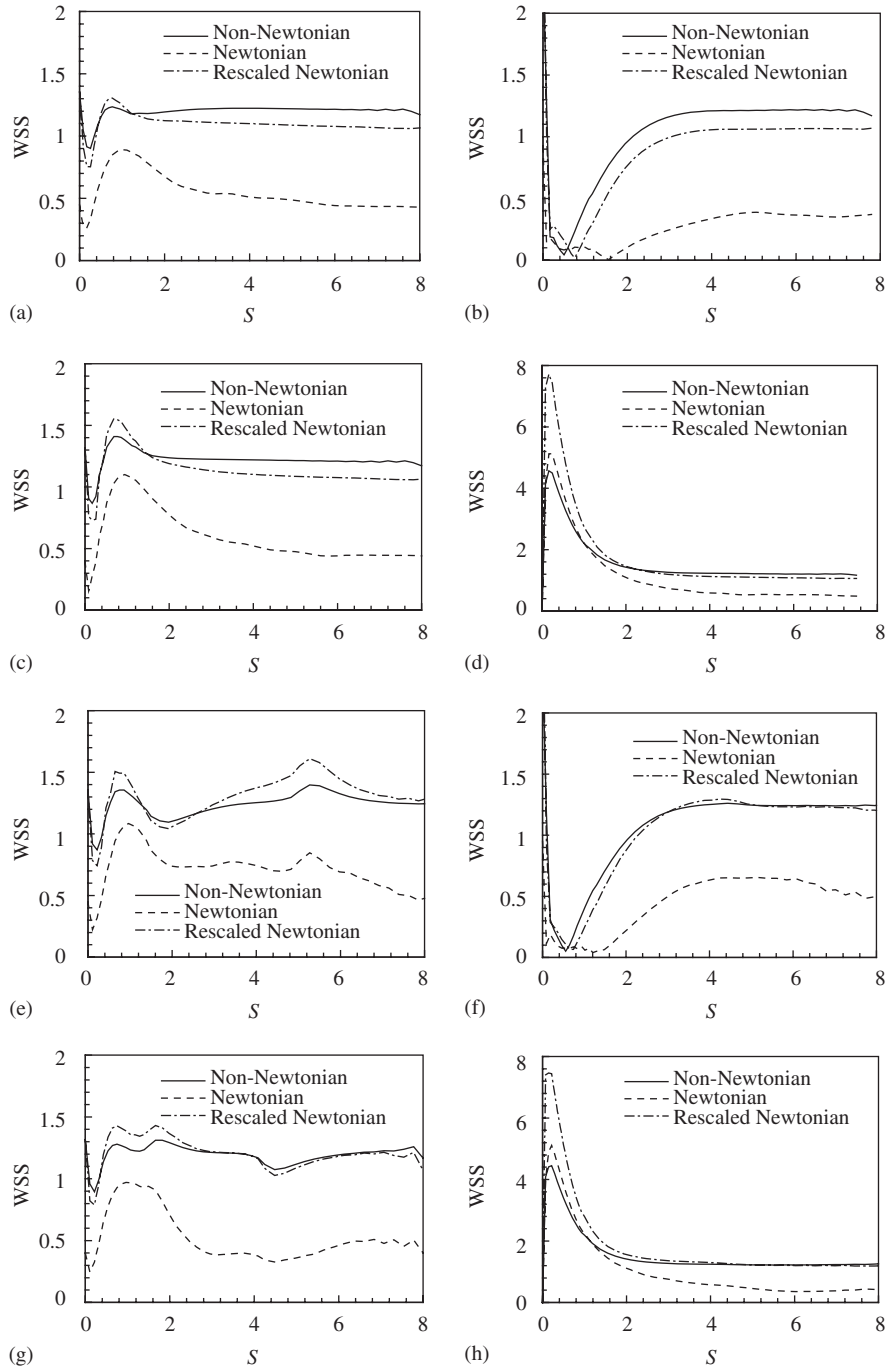


Fig. 10. Distributions of WSS along eight generating lines on the daughter vessels at the end of diastole: (a) A–A'; (b) B–B'; (c) C–C'; (d) D–D'; (e) 1–1'; (f) 2–2'; (g) 3–3'; (h) 4–4'.

wall of the bend in Fig. 10(e), the opposite behavior occurs, and the WSS over the section of the bend is increased on average by 10–15% compared to that in the planar vessel in Fig. 10(a). These findings agree well with the changes in flow distributions caused by the out-of-planar bend and correspond to the rotation of the axial flow in the curved branch. It is noted that the WSS of the non-Newtonian flow agrees well with that of the

rescaled Newtonian flow but is, however, higher than that of the Newtonian flow.

Further, viewing WSS profiles at the inner and the outer walls of the bifurcation plane in Fig. 10, it is seen that peak WSS exists on the inner wall in the bifurcation plane near the entry section of the daughter vessel in Fig. 10(d) and (h). The profiles of WSS predicted by the non-Newtonian and Newtonian flow are similar for

$S < 1.5$ but exhibit significant difference for $S > 1.5$. The WSS profiles of the rescaled Newtonian flow depict a higher peak at $S = 0.3$ approximately and agree with that of the non-Newtonian flow for $S > 1.5$. At the outer wall of the bifurcation plane in Fig. 10(b) and (f), the WSS is nearly close to zero at $S = 0.5$ approximately for the non-Newtonian and the rescaled Newtonian flow and at $S = 1.5$ for the Newtonian flow. The distribution of WSS of the non-Newtonian flow is higher than that

of the Newtonian flow for $S > 1.5$. Meanwhile, note that, as shown in Fig. 8(b) and (f) for the WSS profiles at peak systole, the WSS for the non-Newtonian, Newtonian and the rescaled Newtonian flow are identically close to zero for $S = 1–1.2$ approximately.

Distributions of OSI along four generating lines on the non-planar and planar daughter vessels are shown in Fig. 11. The peak OSI distributions (i.e., high shear stress temporal oscillations) are formed along the outer

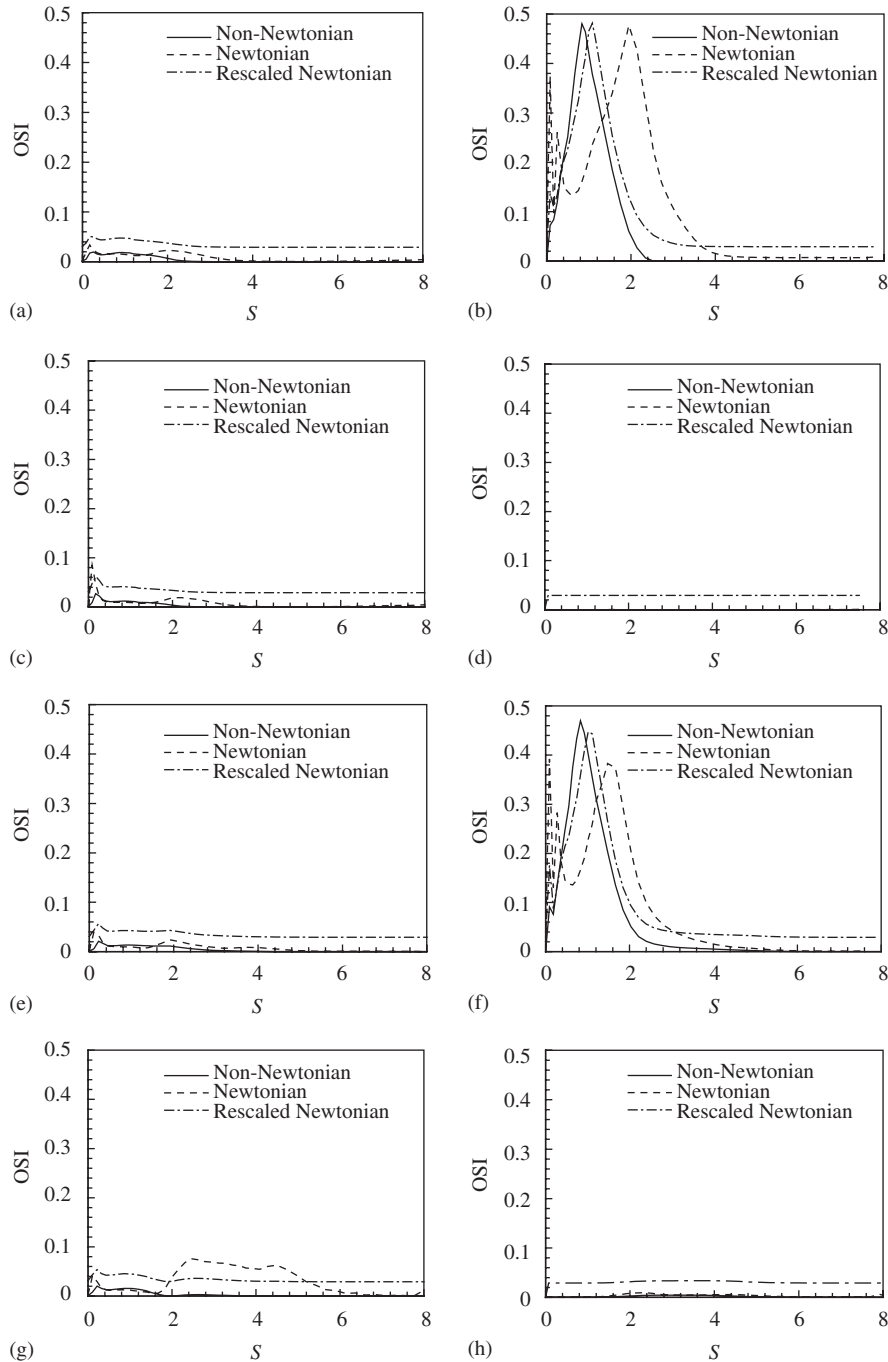


Fig. 11. Distributions of OSI along eight generating lines on the daughter vessels for the non-Newtonian (solid line), Newtonian (dashed line) and rescaled Newtonian fluid flow (dash-dot line): (a) A–A'; (b) B–B'; (c) C–C'; (d) D–D'; (e) 1–1'; (f) 2–2'; (g) 3–3'; (h) 4–4'.

wall of the bifurcation plane in Fig. 11(b) and (f). Correspondingly, low shear stress temporal oscillations are generated along other generating lines (except for generating lines B–B' and 2–2') on the non-planar and planar daughter vessels.

4. Discussion and conclusion

Flow separation, recirculation, as well as low and oscillating wall shear stress are decisive atheromatic factors. Using both in vivo and in vitro models, it has been found that vessels, which are prone to plaque formation, have the flow patterns characterized by low wall shear stress (WSS), flow separation and stasis, and oscillations of flow (Araim et al., 2001). The appearance of low WSS usually coincides with early intimal thickening in the carotid artery (Ku et al., 1985) and abdominal aorta (Moore et al., 1994). Meanwhile, the complex configuration of the vessel promotes flow separation and vortex formation, where complex flow features appear with low time-averaged WSS and high shear stress temporal oscillations during the pulse cycle.

Based on the WSS profiles along the outer wall of the bifurcation plane (i.e., generating lines B–B' and 2–2') in Figs. 8–10, the WSS approaches near to zero in the region of $S = 0.5$ – 1.5 approximately during the pulse cycle. In the same zone, high shear stress temporal oscillations, measured by oscillatory shear index (OSI) in Fig. 11(b) and (f), appear at $S = 1$ approximately for the non-Newtonian and the rescaled Newtonian flow and at $S = 2$ for the Newtonian flow. Further, as shown in Figs. 3–5, flow separation is evident near the outer walls of the vessels in the bifurcation plane at $S \leq 1.5$. Based on these results, we can find that a recirculation zone is observed on the outer wall region of the daughter vessels close to the bifurcation, and low time-averaged WSS and high shear stress temporal oscillations (or OSI) occur too. The outer wall regions of the daughter vessels close to the bifurcation may be associated with localized disease as pointed out by Caro et al. (1978) and Pedley (1980).

During the pulse cycle, some typical flow phenomena occur in Figs. 3–5. The characteristics shown in Fig. 5 are similar to those for steady flow (Chen and Lu, 2004). This behavior was also verified by Gijsen et al. (1999b). At peak systole, the time-dependent part of the elastic stress tensor could influence the flow features; however, the time-dependent viscoelastic properties of the analog blood fluid are not important for the velocity distribution in their specific case (Gijsen et al., 1999b). Thus, the present calculated results are reasonable for understanding the non-Newtonian flow behaviors under unsteady flow conditions.

The pulsatile flow intensifies the phenomenon of separation and flow reversal (Taylor et al., 1998, 1999).

During the pulse cycle, low WSS values appear in the outer wall regions of the daughter vessels. Even at high inlet flow velocities (e.g., peak systole), in these regions, the wall shear stress remains relatively low compared to the values at the flow divider. The distribution pattern of low and oscillating WSS is reasonably close to the development of atherosclerotic lesions.

The non-planarity of artery has an important influence on arterial flows (Caro et al., 1996). Considering the fully developed flow field in a helically symmetric tube, secondary flow changes from a single vortex to a pair of symmetrical vortices (Dean flow) as the Dean number increases, and shear stress reduces by increasing the non-planarity of the helical tube. As shown in Figs. 6 and 7, secondary flows that swirl fluid from the inner wall of curvature to the outer wall along the vessels have been well documented for curved and bifurcating vessels. At sections close to the bifurcation, the Dean vortices are evident and result in a shift of the peak axial velocity toward the flow-dividing wall. These results agree well with the observations predicted by Zabielsky and Mestel (1998a, b) and support the hypothesis of Kamiya and Togawa (1980) that arteries adapt their shape in order to reduce excessive WSS.

Local hemodynamic patterns are also dependent on the rheological properties of blood. As exhibited early, a significant difference between the velocity distributions for the Newtonian and non-Newtonian fluid is evident. The non-Newtonian fluid shows a flattened axial velocity profile due to its shear thinning behavior and has lower velocity gradients at the divider wall and positive velocity gradients at the non-divider wall. However, the curvature-induced secondary flow seems to be less dominant for the non-Newtonian fluid.

The shear thinning behavior of the blood allows for approximation by a viscosity evaluated at the characteristic shear rate of the flow. The results, including the flow field, WSS, and OSI in the daughter vessels, of the rescaled Newtonian pulsatile flow compare well to those of the non-Newtonian pulsatile flow. Usually, the definition of the characteristic shear rate is under dispute. Based on the present calculated results, the agreement between the non-Newtonian and rescaled Newtonian velocity field indicates that a definition of the characteristic shear rate, based on an average shear rate, as proposed by Thurston (1979), Baaijens et al. (1993) and Gijsen et al. (1999a, b), is appropriate.

The rescaled Newtonian fluid model underestimates WSSs in low wall shear rate regions and overestimates WSSs in high shear rate regions, as shown in Figs. 8–10 for the profiles of WSS of the non-Newtonian flow. Actually, as indicated by Gijsen et al. (1999a, b), application of the rescaled Newtonian fluid is hard to be generalized to all geometries and flow conditions. Based on our calculated results, the WSS of the rescaled

Newtonian flow is reasonably consistent with the data of the non-Newtonian flow along the daughter vessels.

Furthermore, the sensitivity to the characteristic shear rate could also help to explain the difference between the flow fields in younger and older individuals (Reneman et al., 1985). As the characteristic shear rate in the older individuals is lower, the characteristic viscosity is higher. Thus, the absence of flow reversal in the internal carotid artery in the older individuals could be explained. However, the characteristic shear rate is higher for younger individuals, and blood is therefore expected to behave more like a Newtonian fluid flow.

The main findings of this study can be summarized as follows. The non-Newtonian property in the daughter vessels induces a flattened axial velocity profile due to its shear thinning behavior during the pulse cycle. The non-planarity in the daughter vessel deflects flow from the inner wall of the vessel to the outer wall and alters the distribution of WSS along the vessel. Downstream of the bifurcation, the velocity profiles are shifted toward the flow divider, and low WSS and high shear stress temporal oscillations characterized by OSI appear on the outer wall zone of the daughter vessels close to the bifurcation. Secondary motions with the fluid from the outer wall of the bifurcation toward the inner wall become stronger with the addition of the out-of-plane curvature induced by the bending of the vessel, and secondary flow patterns swirl along the non-planar daughter vessel. However, the curvature-induced secondary flow seems to be less dominant for the non-Newtonian fluid. The appearance of the low WSS and high OSI is to coincide with early intimal thickening in the carotid artery and abdominal aorta. All these findings suggest that the non-Newtonian properties of blood and the non-planarity in blood vessels are important in the hemodynamic effect. They affect the interaction between flows and the vessel and are likely to alter the residence time of particles and biological cells in the close vicinity of the vascular endothelium, and may thus play an important role in vascular biology and pathophysiology.

Acknowledgements

This work was supported by the Outstanding Overseas Chinese Scholars Fund of Chinese Academy of Sciences, the National Natural Science Foundation (No. 10028205), and the Hundred-Talent Programme of Chinese Academy of Sciences.

References

- Araim, O., Chen, A.H., Sumpio, B., 2001. Hemodynamic forces: effects on atherosclerosis. *New Surgery* 1, 92–100.
- Baaijens, J.P.W., van Steenhoven, A.A., Janssen, J.D., 1993. Numerical analysis of steady generalized Newtonian flow in a 2D model of the carotid artery bifurcation. *Biorheology* 30, 63–74.
- Ballyk, P.D., Steinman, D.A., Ethier, C.R., 1994. Simulation of non-Newtonian blood flow in an end-to-side anastomosis. *Biorheology* 31, 565–586.
- Bassiouny, H.S., White, S., Glagov, S., Choi, E., Giddens, D.P., Zarins, C.K., 1992. Anastomotic intimal hyperplasia: mechanical injury or flow induced. *Journal of Vascular Surgery* 15, 708–717.
- Bird, R.B., Armstrong, R.C., Hassager, O., 1987. , second ed. *Dynamics of Polymer Liquids*, vol. 1. Wiley, New York.
- Caro, C.G., Baker, A.J., Fitzgerald, J.M., Schroter, R.C., 1971. Atheroma and arterial wall shear: observations, correlation and proposal of a shear dependent mass transfer mechanism for atherogenesis. *Proceedings of the Royal Society of London B* 117, 109–159.
- Caro, C.G., Pedley, T.J., Schroter, R.C., Seed, W.A., 1978. *The Mechanics of the Circulation*. Oxford University Press, Oxford.
- Caro, C.G., Doorly, D.J., Tarnawski, M., Scott, K.T., Long, Q., Dumoulin, C.L., 1996. Non-planar curvature and branching of arteries and non-planar-type flow. *Proceedings of the Royal Society of London B* 452, 185–197.
- Chen, J., Lu, X.Y., 2004. Numerical investigation of the non-Newtonian blood flow in a bifurcation model with a non-planar branch. *Journal of Biomechanics* 37, 1899–1911.
- Chien, S., Usami, S., Dellenback, R.J., Gregersen, M.I., 1970. Sheardependent deformation of erythrocytes in rheology of human blood. *American Journal of Physiology* 219, 136–142.
- Cho, Y.I., Kensey, R., 1991. Effects of the non-Newtonian viscosity of blood flows in a diseased arterial vessel, Part 1: Steady flows. *Biorheology* 28, 241–262.
- Delfino, A., Stergiopoulos, N., Moore Jr., J.E., Meister, J.J., 1997. Residual strain effects on the field in a thick wall finite element model of the human carotid bifurcation. *Journal of Biomechanics* 30, 777–786.
- Ding, Z.R., Wang, K.Q., Li, J., Cong, X.S., 2001. Flow field and oscillatory shear stress in a tuning-fork-shaped model of the average human carotid bifurcation. *Journal of Biomechanics* 34, 1555–1562.
- Dobrin, P.B., Littooy, F.N., Endean, E.D., 1989. Mechanical factors predisposing to intimal hyperplasia and medial thickening in autogenous vein grafts. *Surgery* 105, 393–400.
- Friedman, M.H., Ding, Z.H., 1998. Variability of the planarity of the human aortic bifurcation. *Medical Engineering and Physics* 20, 469–472.
- Friedman, M.H., Peters, O.J., Barger, C.B., Hutchins, G.M., Mark, F.F., 1981. Correlation between intimal thickness and fluid shear in human arteries. *Atherosclerosis* 39, 425–436.
- Gijzen, F.J.H., van de Vosse, F.N., Janssen, J.D., 1999a. The influence of the non-Newtonian properties of blood on the flow in large arteries: steady flow in a carotid bifurcation model. *Journal of Biomechanics* 32, 601–608.
- Gijzen, F.J.H., van de Vosse, F.N., Janssen, J.D., 1999b. The influence of the non-Newtonian properties of blood on the flow in large arteries: unsteady flow in a 90° curved tube. *Journal of Biomechanics* 32, 705–713.
- Hofer, M., Rappitsch, G., Perktold, K., Turbel, W., Schima, H., 1996. Numerical study of wall mechanics and fluid dynamics in end-to-side anastomoses and correlation to intimal hyperplasia. *Journal of Biomechanics* 29, 1297–1308.
- Hughes, P.E., How, T.V., 1995. Flow structures at the proximal side-to-end anastomosis: influence of geometry and flow division. *Journal of Biomechanical Engineering* 117, 224–236.
- Kamiya, A., Togawa, T., 1980. Adaptive regulation of wall shear stress to flow change in the canine artery. *American Journal of Physiology* 239, H14–H21.

- Kleinstreuer, C., Lei, M., Archie, J.P., 1996. Flow input waveform effects on the temporal and spatial wall shear stress gradients in a new femoral graft-artery connector. *Journal of Biomechanical Engineering* 118, 506–510.
- Kovacs, A., Kawahara, M., 1991. A finite element scheme based on the velocity correction method for the solution of the time-dependent incompressible Navier–Stokes equations. *International Journal for Numerical Methods in Fluids* 13, 403–423.
- Ku, D.N., Liepsch, D., 1986. The effect of non-Newtonian viscoelasticity and wall elasticity on flow at a 90° bifurcation. *Biorheology* 23, 359–370.
- Ku, D.N., Giddens, D.P., Zarins, C.K., Glagov, S., 1985. Pulsatile flow and atherosclerosis in the human carotid bifurcation: positive correlation between plaque location and low and oscillating shear stress. *Atherosclerosis* 5 (3), 293–302.
- Lee, D., Su, J.M., Liang, H.Y., 2001. A numerical simulation of steady flow fields in a bypass tube. *Journal of Biomechanics* 34, 1407–1416.
- Lei, M., Archie, J.P., Kleinstreuer, C., 1997. Computational design of a bypass graft that minimizes wall shear stress gradients in the region of the distal anastomosis. *Journal of Vascular Surgery* 25, 637–646.
- Liepsch, D., Moravec, S., 1984. Pulsatile flow of non-Newtonian fluid in distensible models of human arteries. *Biorheology* 21, 571–586.
- Lou, Z., Yang, W.J., 1993. A computer simulation of the non-Newtonian blood flow at the aortic bifurcation. *Journal of Biomechanics* 26, 37–49.
- Lu, Y.L., Lu, X.Y., Zhuang, L.X., Wang, W., 2002. Breaking symmetry in non-planar bifurcation: distribution of flow and wall shear stress. *Biorheology* 39, 431–436.
- Mann, D.E., Tarbell, J.M., 1990. Flow of non-Newtonian blood analog fluids in rigid curved and straight artery models. *Biorheology* 27, 711–733.
- Moore Jr., J.E., Xu, C., Glagov, S., Zarins, C.K., Ku, D.N., 1994. Fluid wall shear stress measurements in a model of the human abdominal aorta: oscillatory behavior and the relationship to atherosclerosis. *Atherosclerosis* 110, 225–240.
- Nerem, R.M., 1992. Vascular fluid mechanics, the arterial wall, and atherosclerosis. *Journal of Biomechanical Engineering* 114, 274–282.
- Ojha, M., 1994. Wall shear stress temporal gradient and anastomotic intimal hyperplasia. *Circulation Research* 74, 1227–1231.
- Pedley, T.J., 1980. *The Fluid Mechanics of Large Blood Vessels*. Cambridge University Press, Cambridge.
- Perktold, K., Hofer, M., Rappitsch, G., Loew, M., Kuban, B.D., Friedman, M.H., 1998. Validated computation of physiologic flow in a realistic coronary artery branch. *Journal of Biomechanics* 31, 217–228.
- Reneman, R.S., van Merode, T., Hick, P., Hoeks, A.P.G., 1985. Flow velocity patterns in and distensibility of the carotid artery bulb in subjects of various ages. *Circulation* 71 (3), 500–509.
- Santamarina, A., Weydahl, E., Siegel Jr., J.M., Moore Jr., J.E., 1998. Computational analysis of flow in a curved tube model of the coronary arteries: effects of time-varying curvature. *Annals of Biomedical Engineering* 26, 944–954.
- Sarkar, A., Jayaraman, G., 1998. Correction to flow rate—pressure drop relation in coronary angioplasty: steady streaming effect. *Journal of Biomechanics* 31, 781–791.
- Schwartz, L.B., O'Donohoe, M.K., Purut, C.M., Mikat, E.M., Hagen, P.O., McCann, R.L., 1992. Myointimal thickening in experimental vein grafts is dependent on wall tension. *Journal of Vascular Surgery* 15, 176–186.
- Sherwin, S.J., Shah, O., Doorly, D.J., Peiro, J., Papaharilou, Y., Watkins, N., Caro, C.G., Dumoulin, C.L., 2000. The influence of out-of-plane geometry on the flow within a distal end-to-side anastomosis. *Journal of Biomechanical Engineering* 122, 86–95.
- Shipkowitz, T., Rodgers, V.G.J., Franzin, L.J., Chandran, K.B., 1998. Numerical study on the effect of steady axial flow development in the human aorta on local shear stresses in abdominal. *Journal of Biomechanics* 31, 995–1007.
- Staalsen, N.H., Vlrich, M., Winther, J., Pederson, E.M., How, T., Nygaard, H., 1995. The anastomosis angle does change the flow fields at vascular end-to-side anastomoses in vivo. *Journal of Vascular Surgery* 21, 460–471.
- Taylor, C.A., Hughes, T.J.R., Zarins, C.K., 1998. Finite element modeling of three-dimensional pulsatile flow in the abdominal aorta: relevance to atherosclerosis. *Annals of Biomedical Engineering* 26, 975–987.
- Taylor, C.A., Hughes, T.J.R., Zarins, C.K., 1999. Effect of exercise on hemodynamic conditions in the abdominal aorta. *Journal of Vascular Surgery* 29, 1077–1089.
- Thurston, G.B., 1973. Frequency and shear rate dependence of viscoelasticity of human blood. *Biorheology* 10, 375–381.
- Thurston, G.B., 1979. Rheological parameters for the viscosity, viscoelasticity and thixotropy of blood. *Biorheology* 16, 149–162.
- Tu, C., Deville, M., 1996. Pulsatile flow of non-Newtonian fluids through arterial stenoses. *Journal of Biomechanics* 29, 899–908.
- Wang, Y.X., Lu, X.Y., Zhuang, L.X., 2004. Numerical analysis of the rotating viscous flow approaching a solid sphere. *International Journal for Numerical Methods in Fluids* 44, 905–925.
- Weston, S.J., Wood, N.B., Tabor, G., Gosman, A.D., Firmin, D.N., 1998. Combined MRI and CFD analysis of fully developed steady and pulsatile laminar flow through a bend. *Journal of Magnetic Resonance Imaging* 8, 1158–1171.
- Weydahl, E.S., Moore Jr., J.E., 2001. Dynamic curvature strongly affects wall shear rates in a coronary artery bifurcation model. *Journal of Biomechanics* 34, 1189–1196.
- White, S.S., Zarins, C.K., Giddens, D.P., Bassiouny, H., Loth, F., Jones, S.A., Glagov, S., 1993. Hemodynamic patterns in two models of end-to-side vascular graft anastomoses: effects of pulsatility, flow division, Reynolds number, and hood length. *Journal of Biomechanical Engineering* 115, 104–111.
- Zabielsky, L., Mestel, J., 1998a. Steady flow in a helically symmetric pipe. *Journal of Fluid Mechanics* 370, 297–320.
- Zabielsky, L., Mestel, J., 1998b. Unsteady blood flow in a helically symmetric pipe. *Journal of Fluid Mechanics* 370, 321–345.
- Zarins, C.K., Giddens, D.P., Bharadvaj, B.K., Sottiurai, V., Mabon, R.F., Glagov, S., 1983. Carotid bifurcation atherosclerosis: quantitative correlation of plaque localization with flow velocity profiles and wall shear stress. *Circulation Research* 53, 502–514.
- Zendehbudi, G.R., Moayeri, M.S., 1999. Comparison of physiological and simple pulsatile flows through stenosed arteries. *Journal of Biomechanics* 32, 959–965.
- Zhao, S.Z., Xu, X.Y., Hughes, A.D., Thom, S.A., Stanton, A.V., Ariff, B., Long, Q., 2000. Blood flow and vessel mechanics in a physiologically realistic model of a human carotid arterial bifurcation. *Journal of Biomechanics* 33, 975–984.